

Simulation of terahertz generation at semiconductor surfaces

M. B. Johnston, D. M. Whittaker, A. Corchia, A. G. Davies, and E. H. Linfield

University of Cambridge, Cavendish Laboratory, Madingley Road, Cambridge CB3 0HE, United Kingdom

(Received 8 October 2001; published 18 March 2002)

A three-dimensional semiclassical Monte Carlo model is presented to describe fast carrier dynamics in semiconductors after photoexcitation. Far-field terahertz (THz) radiation patterns are calculated for both InAs and GaAs with, and without, application of external magnetic fields. This analysis distinguishes between surface depletion field and photo-Dember mechanisms for generating THz radiation. The theoretical model reproduces experimental data from GaAs and InAs, and demonstrates that a magnetic field enhances THz emission by rotating the emitting dipole with respect to the sample surface, leading to an increased coupling of radiation through the surface.

DOI: 10.1103/PhysRevB.65.165301

PACS number(s): 78.47.+p, 73.20.Mf, 78.20.Bh

I. INTRODUCTION

Coherent terahertz (THz) frequency radiation is emitted from the surface of a semiconductor after excitation by an ultrafast laser pulse.^{1,2} Observing the resulting electric-field transients provides a powerful, noncontact method of studying hot carrier dynamics,³ collective processes,⁴ and material properties of semiconductors with subpicosecond time resolution. Currently, there is considerable interest in exploiting these transients for the emerging applications of coherent THz spectroscopy^{5,6} and imaging.^{7,8}

The mechanism by which THz radiation is generated when semiconductor surfaces are illuminated with near-infrared laser pulses is an issue of debate.^{9–11} InAs has been shown to emit THz transients with an order of magnitude more power than commonly used wide band-gap semiconductors, such as InP and GaAs, under similar conditions.^{12,13} Furthermore, it has been observed recently that application of an external magnetic field causes an order of magnitude enhancement of THz emission from a variety of semiconductor surfaces (InAs, InSb, GaSb, GaAs, InP).^{12–16,18,17}

In this paper we present a complete theoretical study of THz generation from both InAs and GaAs with, and without, application of an external magnetic field. Our model describes carrier dynamics in three dimensions, as well as propagation of the THz field inside and outside the semiconductor. Thus with one model we are able to reproduce and explain the differences between THz generation from different semiconducting materials, as well as the absolute enhancement of radiated THz power with magnetic field.

After discussion of the theoretical background to our work in Sec. II A, we describe in Sec. II B our three-dimensional semiclassical Monte Carlo carrier dynamics simulation. Section III details the use of this simulation to show that, under the typical excitation condition attainable with a Ti:sapphire laser, emission from InAs is almost entirely produced by the photo-Dember effect, whereas emission from GaAs results mostly from a surface depletion field generation mechanism. Finally in Sec. IV, the enhancement in emitted THz power with magnetic field is discussed in terms of dipole rotation and Fresnel transmission coefficients.

II. THEORY

A. Background

After photoexcitation, surfaces of bulk semiconductors generate THz radiation primarily as the result of two processes: *ultrafast charge transport* and *difference frequency mixing* (“optical rectification”).^{19–21} In this study we focus on charge transport, since the polarization effects leading to optical rectification are negligible for the crystal orientations and photon energies used in the experimental results we discuss.^{9–12,14–16}

Ultrafast charge transport is driven by the intrinsic surface electric field of the semiconductor^{22,23} and/or by a difference in the mobilities of the electrons and holes (photo-Dember effect).^{24–27,9,10} The resulting charge separation, and the subsequent carrier motion it initiates, leads to the emission of a THz transient. The carrier motion, and hence the form of the THz transient, depends on the density distribution and interactions between extrinsic and photoexcited carriers, as well as magnetoplasmon effects.

Previously, theoretical studies of the photo-Dember effect have been performed by Efanov and Éntin²⁸ using the diffusion equation, and by Held *et al.*²⁹ using a hydrodynamic model. Furthermore, Dekorsy *et al.*,²³ with a drift diffusion treatment, simulated carrier dynamics in the surface electric field of GaAs, with Kersting *et al.*^{30,4} then using this approach to model THz emission from GaAs. A quantum-mechanical approach was also developed by Kuznetsov and Stanton³¹ to investigate THz emission from both GaAs and InP in a constant electric field. However, none of these one-dimensional analyses explain quantitatively the observed THz spectra because of the nonuniform laser beam intensity cross section and rapid in-plane carrier diffusion.

Modeling systems which include the influence of an external magnetic field necessarily requires a full three-dimensional analysis, since the field will alter the charge-density distribution in the plane perpendicular to the velocity of the carriers. Efanov and Éntin³² derived analytic expressions for a magnetic-field-induced enhancement of the photo-Dember effect for the specific case of a weak magnetic field parallel to the surface of the semiconductor. Meinert *et al.*³³ then used a quantum-mechanical approach to discuss

the importance of LO phonon scattering on THz emission in crossed electric and magnetic fields, and Heyman *et al.*¹⁷ used a three-dimensional Drude-Lorentz approach to model the magnetic-field dependence of THz power emitted from GaAs and InAs. However, these studies neglected the propagation of THz radiation through the dielectric interface which determines the absolute magnetic-field-induced power enhancement for both GaAs and InAs.^{18,34} Shan *et al.*¹⁸ showed the importance of this dielectric interface on the magnetic-field enhancement of THz emission from semiconductors. However, their model of damped cyclotron motion did not account for the photo-Dember mechanism or magnetoplasmon effects.

Here we present a single model, based on a three-dimensional Monte Carlo simulation, which explains the relative importance of surface-field and photo-Dember THz generation mechanisms in different semiconductor systems, and gives quantitative agreement with the observed magnetic-field-induced power enhancements. It includes interactions between extrinsic carriers and photogenerated carriers, the effects of plasmon and magnetoplasmons, and the role played by the dielectric-air interface.

B. Model

In our Monte Carlo dynamics model we use the time derivative of the total current as a source term in Maxwell's equations, which allows us to reproduce the electric-field wave forms (and hence spectra) of the THz frequency transient produced from semiconductor surfaces in the presence of an external magnetic field.

The simulation volume is divided into a three-dimensional rectangular mesh, and the motion of electrons and holes are calculated over small time intervals, $\Delta t = 2$ fs, much less than the scattering time. In each small time and space interval, all fields are assumed to be constant and uniform and the motion of each carrier is calculated according to the analytic solutions of

$$\ddot{\mathbf{r}}(\mathbf{r}, t) = \frac{q_e}{m^*} [\mathbf{E}_\phi(\mathbf{r}, t) + \dot{\mathbf{r}}(\mathbf{r}, t) \times \mathbf{B}], \quad (1)$$

where $\ddot{\mathbf{r}}$ and $\dot{\mathbf{r}}$ are the acceleration and velocity of the electron (hole) with charge q_e and effective mass m^* in an electric field \mathbf{E}_ϕ and magnetic field \mathbf{B} . Then a set of scattering rates W_i are calculated for each particle in the simulation from the particle's energy and the local electron/hole density. Random numbers are used to determine if the particle will scatter in that time interval, and the resulting scattering angle (see Sec. II C).

After each small time interval the electron and hole density meshes are updated and are used to find the electric potential Φ by solving Poisson's equation on the three-dimensional (3D) mesh using a relaxation method with Chebyshev acceleration.³⁵ The electric-field vector \mathbf{E}_ϕ , used in Eq. (1), is determined from $\mathbf{E}_\phi = -\nabla\Phi$, using the central difference method for the mesh box containing the particle.

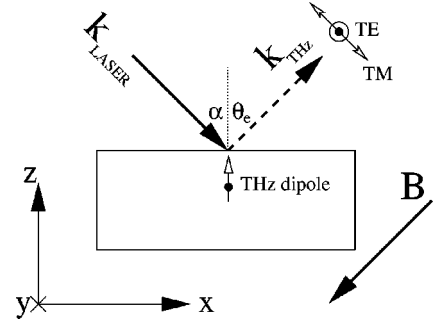


FIG. 1. Schematic diagram of the experimental geometry and coordinate system used for all simulations. A femtosecond laser pulse is incident on the surface of a semiconductor at an angle α . The radiation is absorbed in the surface region of the semiconductor leading to the formation of a THz dipole. Emitted THz radiation is measured as a function of the angle θ_e . The direction of the applied magnetic field is represented by the vector labeled \mathbf{B} .

The potential at the surface boundary of the semiconductor is fixed to the pinning potential [$\Phi(x, y, z=0) = \Phi_s$] and the Neumann boundary condition of $\partial\Phi/\partial z = 0$ is used for the parallel boundary between the simulation volume and the rest of the substrate. Cyclic boundary conditions are applied to the other four boundaries. For the simulations presented in this paper, the semiconductor surface is assumed to be perfectly reflecting for electrons and holes.

Arbitrary excitation, detection, and magnetic-field geometries may be used in the simulation, however, for this paper we will restrict calculations to the geometry shown in Fig. 1.

Initially, our model calculates the distribution of extrinsic electrons/holes. A first-order estimate of this distribution is obtained from the value of the surface potential (a simulation parameter). The temperature of these (“cold”) carriers is initially set to be that of the lattice, and the simulation runs until an equilibrium charge distribution (and hence surface electric field) is established.

The inclusion of thermalized extrinsic carriers in the simulation is an important point. The surface electric-field profile, which is critical to the surface field-emission mechanism, is very sensitive to the dynamics of these cold carriers. Indeed it has also been shown experimentally that “cold plasmon” oscillations contribute significantly to the THz emission process.³⁰

The simulation then generates photoexcited carriers according to the spatial and temporal intensity of the femtosecond laser pulse absorbed at the sample surface. A pseudorandom number generator is used to calculate the initial spatial positions of each electron-hole pair. The distribution in the z direction is weighted exponentially as defined by the absorption coefficient of the light in the semiconductor. The distribution in the x - y plane is weighted to reflect the Gaussian profile of the laser-pulse intensity.

The initial energy of the electron-hole pairs is the difference between the semiconductor band gap and the photon energy, and the energy is partitioned between electrons and holes based on momentum conservation. For simplicity, parabolic dispersions are assumed for electron and hole

bands. The directions of the momentum vectors are initially randomized with equal probability across 4π steradians.

In order to obtain the THz electric field radiated by the ensemble, the time derivative of the net current,

$$\frac{\partial \mathbf{J}}{\partial t} = \sum_i q_i \ddot{\mathbf{r}}_i, \quad (2)$$

is calculated as a function of time. It acts as the source term in Maxwell's equations when determining the THz emission. The calculation of emission through the dielectric boundary at the surface of the semiconductor is presented in Sec. IV B.

C. Scattering

The results of the simulation are particularly sensitive to carrier scattering. We included four forms of scattering in our simulation, namely: polar and nonpolar optical-phonon scattering, impurity scattering, and carrier-carrier scattering.

The most important scattering mechanisms for photoexcited "hot" carriers are polar optical-phonon scattering and nonpolar optical-phonon mediated scattering between the Γ and L valleys. Phonon emission is the main form of dissipation in the Monte Carlo ensemble. An expression for the polar optical-phonon scattering rate for absorption and emission processes, W_p , is obtained by application of Fermi's golden rule with the Fröhlich interaction, giving³⁶

$$W_p(k) = \frac{q_e^2 \omega_0}{8\pi\epsilon_p} \frac{k}{E_k} \left(f_B(\hbar\omega_0) + \frac{1}{2} \mp \frac{1}{2} \right) \ln \left(\frac{k_{max}}{k_{min}} \right), \quad (3)$$

with

$$k_{max} = k \left| 1 - \left(1 \pm \frac{\hbar\omega_0}{E_k} \right)^{1/2} \right|, \quad (4)$$

$$k_{min} = k \left[1 + \left(1 \pm \frac{\hbar\omega_0}{E_k} \right)^{1/2} \right]. \quad (5)$$

ω_0 designates the angular frequency of the phonon, while k and E_k are the initial magnitude of the wave vector and energy, respectively, for an electron with wave vector \mathbf{k} . $1/\epsilon_p = 1/\epsilon_\infty - 1/\epsilon_0$, where ϵ_∞ and ϵ_0 are the high- and low-frequency limits of the permittivity of the sample, and $f_B(\hbar\omega_0)$ is the Bose-Einstein distribution function.

For polar optical-phonon scattering the azimuthal scattering angle (ϕ) is determined by generating an evenly distributed random number between 0 and 2π , whereas the polar scattering angle (θ) distribution function is derived from the function

$$W_p(\theta) = \frac{\ln[k(\theta)/k_{min}]}{\ln(k_{max}/k_{min})} W_p(k), \quad (6)$$

which gives the probability of scattering between 0 and θ . k and $k(\theta)$ are the magnitude of wave vectors before and after scattering, respectively.

Scattering of carriers between Γ and L valleys via nonpolar phonon absorption and emission is particularly important when modeling hot carriers in narrow band-gap semiconductors. In such cases the assumption of parabolic bands is not valid. However, inclusion of scattering between the Γ and L valleys creates a more realistic ensemble average effective mass and carrier temperature. The scattering rate, which has been derived in Ref. 36, is

$$W(k)_{\Gamma=L} = \frac{\pi \hbar^2 \sqrt{q_e}}{\omega_L \rho} \beta d_L^2 D(E_{f(\Gamma=L)}) \left(f_B(\hbar\omega_L) + \frac{1}{2} \mp \frac{1}{2} \right), \quad (7)$$

where $D(E_f)$ is the density of final electron states with energy $E_{f(\Gamma \rightarrow L)} = E_k \pm \hbar\omega_L - E_{L-\Gamma}$ and $E_{f(L \rightarrow \Gamma)} = E_k \pm \hbar\omega_L + E_{L-\Gamma}$. The intervalley deformation potential is d_L , β is the number of final valleys available ($\beta_\Gamma = 1$, $\beta_L = 4$), and ρ is the mass density of the semiconductor. Scattering angle probabilities are evenly distributed over 4π steradians since nonpolar scattering is isotropic.

Impurity scattering is an important mechanism for low energy "cold" carriers. The impurity scattering rate W_{imp} is determined by applying Fermi's golden rule in the Born approximation, where the screened potential is calculated using the Brooks-Herring approach.³⁷ The expression used in the simulation is

$$W_{imp}(k) = \frac{2\pi n_I Z^2 q_e^4 D(E_k)}{\hbar \epsilon_0^2} \frac{1}{k_d^2 (4k^2 + k_d^2)}, \quad (8)$$

where n_I is the density of impurity ions with charge Zq_e and k_d is the inverse Debye length:

$$k_d = \sqrt{\frac{q_e^2 n}{\epsilon k_B T}}, \quad (9)$$

with n the local electron (hole) density.

The polar angle of ionized impurity scattering is generated according to the function:

$$W_{imp}(\theta) = \frac{(1 - \cos \theta)[1 + (2k/k_d)^2]}{2 + (1 - \cos \theta)(2k/k_d)^2} W_p(k), \quad (10)$$

while the azimuthal angle is isotropic.

The carrier-carrier scattering rate is determined according to Eq. (8) with $Z=1$ and replacing n_I with the local hole density. Collective carrier-carrier scattering (plasmon excitation) is included in the simulation through the calculation of the electric potential.

III. TERAHERTZ GENERATION AT SURFACES

A. Introduction: Surface field and photo-Dember mechanisms

If surface energy bands of a semiconductor lie within its bulk band gap, then Fermi level pinning⁴¹ occurs, leading to band bending and the formation of a depletion/accumulation region at the surface. The resulting electric field will separate photogenerated electrons and holes, forming a dipole perpendicular to the surface which emits THz radiation. By changing doping from n type to p type, the sign of the electric-field

TABLE I. Parameters used in GaAs and InAs simulations. Established values taken from Refs. 40,38,39 are used. Excitation is by a 1-nJ, 0.5-mm beam-waist Gaussian pulse of 1.55-eV ($\lambda = 800$ nm) photons in all simulations. The lattice temperature of the semiconductors is set to 300 K, and their doping densities are set to $2 \times 10^{15} \text{ cm}^{-3}$.

	GaAs	InAs
Γ valley effective mass, m^*	$0.067m_0$	$0.022m_0$
L valley effective mass, m_L^*	$0.35m_0$	$0.29m_0$
Hole effective mass, m_h^*	$0.5m_0$	$0.4m_0$
Band-gap energy	1.5 eV	0.35 eV
L valley offset, $E_{L-\Gamma}$	0.29 eV	0.73 eV
LO-phonon energy, $\hbar\omega_L$	0.035 eV	0.030 eV
Mass density ρ	5360 kg m^{-3}	5667 kg m^{-3}
β_L	4	4
β_Γ	1	1
Deformation potential d_L	0.6 eV/\AA	1.4 eV/\AA
ϵ_0	12.95	15.5
ϵ_∞	10.9	12.25
α	$1.2 \times 10^4 \text{ cm}^{-1}$	$6.5 \times 10^4 \text{ cm}^{-1}$

direction is reversed. This leads to a change in the polarity of the dipole, which is observed as a change in sign of the generated THz transient.

A photo-Dember field can also occur at the surface of a semiconductor after photoexcitation.^{24–26} Two factors lead to this field: a difference in diffusion coefficients for electrons and holes, and a structural asymmetry. In a typical semiconductor, electrons have a larger diffusion coefficient than holes. Therefore, after photoexcitation, the electron population diffuses more rapidly than the hole population. In the absence of a surface boundary, there would be no net dipole field, since the center of charge does not change. However, in the vicinity of the surface, reflection or capture of charges results in the center of charge for electrons and holes moving away from the surface. A dipole is thus formed perpendicular to the surface, leading to THz emission. In this case changing the semiconductor doping from n to p type has no effect on the sign of the emitted THz pulse.

B. Results: Separation of photo-Dember and surface field mechanisms

Using our model, we studied the carrier dynamics in GaAs and InAs under identical conditions and compared our results with experiments. Simulation parameters and excitation conditions are given in Table I. Figures 2(a) and (b) show the charge distribution for n -type GaAs and InAs, respectively, as a function of depth for different times after photoexcitation.

At $t = -0.25$ ps, prior to the laser pulse hitting the sample, the equilibrium distribution of cold carriers is established. In our simulation we set the surface potential Φ_s of InAs to the conduction-band edge,^{42,43} and to be midgap for GaAs. The surface depletion region, and resulting electric field, of n -type GaAs [Fig. 2(a)] is seen to extend to a depth of over $0.5 \mu\text{m}$. In contrast, for n -type InAs [Fig. 2(b)] a

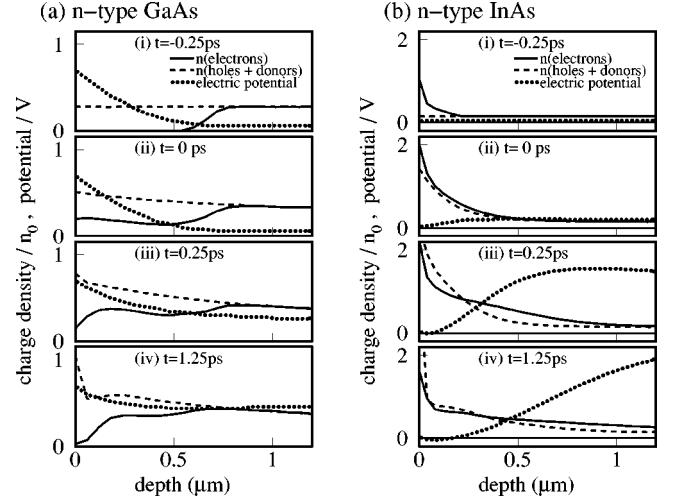


FIG. 2. Average charge carrier distribution as a function of depth from the surface for n -type ($n = 2 \times 10^{15} \text{ cm}^{-3}$) (a) GaAs and (b) InAs at room temperature. The carrier densities have been summed over x - y planes, with scaling unit of $n_0 = 7 \times 10^{15} \text{ cm}^{-3}$. Note that the average density of photoexcited carriers over the whole simulation volume is much lower than the density at the center of the excitation spot. The dotted line shows the average electric potential in volts.

thin layer of electrons accumulates at the surface, and the electric field away from the surface is small.

By $t = 0$ the first half of the laser pulse has been absorbed. For both GaAs and InAs, the exponential absorption profile of the photons is seen as an increase in the electron and hole concentration, which are superimposed on the initial cold carrier distributions. It is significant that in GaAs most carriers are absorbed in the depletion region which has a strong linear electric field, whereas in InAs most absorption occurs in a region of negligible electric field. Note the larger absorption coefficient of InAs for 1.55 eV photons.

By $t = 0.25$ ps, coupling between the hot and cold carriers has begun to occur, and the electron and hole populations separate in both simulations, initiating plasma oscillations. For GaAs, the electron distribution has moved away from the surface and the hole population towards the surface, effectively screening the electric field in the depletion region. For InAs, the electron population broadens and moves away from the surface to a much greater extent than the less mobile hole population. This separation generates a strong photo-Dember field and results in a heavily damped plasma oscillation.

By $t = 1.25$ ps the plasma oscillations have been damped and the depletion field of GaAs is almost totally screened. In InAs charge oscillations have almost ceased, with the drift and diffusion contributions to the current reaching equilibrium. In both cases little more THz radiation is emitted. The much slower electron-hole recombination processes, which are not included in the model, then return the the distributions to the initial ($t = -0.25$ ps) state.

Figure 3 shows the time derivatives of the ensemble average current, $\partial \mathbf{j}_z / \partial t$, for the GaAs and InAs simulations presented in Fig. 2. The THz internal field is proportional to

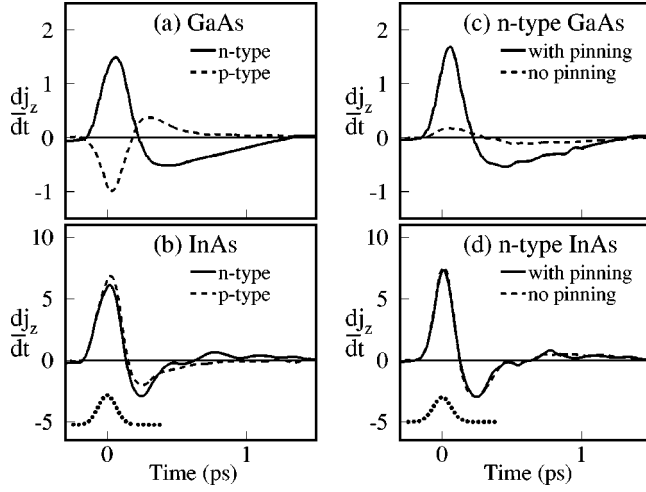


FIG. 3. Time derivatives of the z components of the simulated average current. Graphs (a) and (b) compare n -type (solid lines) and p -type (dashed lines) GaAs and InAs, respectively. Graphs (c) and (d) compare simulations with (solid lines) and without (dashed lines) Fermi-level pinning in (c) n -type GaAs and (d) n -type InAs. The dotted curve represents the intensity profile of the exciting laser pulse.

$\partial \mathbf{j}_z / \partial t$, and has a peak value in n -type InAs which is four times that in n -type GaAs. This $16\times$ power difference agrees well with experiments on similar samples (e.g., $20\times$ in Ref. 12).

Results for simulations of p -type GaAs and InAs are also included in Figs. 3(a) and (b). For p -type GaAs [Fig. 3(a)], the polarity of the THz transient changes sign and the wave form is reduced in amplitude, in good agreement with experiments,^{44,9,27} and suggesting a surface field mechanism. When a similar set of simulations is performed on InAs [Fig. 3(b)], there is only a small change between n -type and p -type samples, again consistent with the experimental results,⁹ which suggests a photo-Dember emission mechanism.

Figures 3(c) and (d) present a more quantitative analysis of the contributions of each generation mechanism to emission from n -type GaAs and InAs. In each plot, the dashed line represents a sample in which the Fermi level is not pinned and so there is no surface depletion field. It therefore represents the pure photo-Dember field emission mechanism. By integrating the power spectra of the GaAs wave forms we find that less than 10% of radiated power is generated by the photo-Dember mechanism. In contrast to GaAs, the n -type InAs wave forms presented in Fig. 3(d) are indistinguishable, indicating close to 100% photo-Dember emission. This occurs because the photoexcited electrons and holes are generated in a region with almost no intrinsic electric field. Even when the doping density is altered, the n -type InAs sample remains a wholly photo-Dember emitter.

On the other hand p -type InAs has a large hole depletion region. Therefore the THz generation mechanism for p -type InAs depends on its surface potential and doping density. Hence there is a difference between p -InAs and n -InAs in Fig. 3(b), but no difference between n -InAs with and without

Fermi level pinning in Fig. 3(d). These results for p -InAs are consistent with a strong photo-Dember mechanism dominating a weaker surface field.

We have also examined (not shown in the figures) the importance of the excess energy of hot photogenerated carriers in InAs by repeating the simulations, but exciting the InAs with 0.4-eV instead of 1.55-eV energy photons (in this case the excess energy is comparable with that in the GaAs simulations). The main effect is an eight times reduction in the amplitude of the time derivative current curves. However, as in Fig. 3(d), there is no significant difference between n -type InAs with and without Fermi-level pinning, indicating that the photo-Dember effect still dominates.

These simulations show that InAs is primarily a *photo-Dember emitter* while GaAs is primarily a *surface field emitter*. The simulations reproduce the large THz electric-field amplitudes (and hence powers) observed experimentally in InAs when compared with GaAs.

IV. MAGNETIC FIELD ENHANCEMENT

The application of a magnetic field to both InAs and GaAs is known to enhance THz emission dramatically. In the geometry shown in Fig. 1, the total power enhancement at 8 T for GaAs is approximately 35 times while for InAs it is about 8.¹³ In order to explain these experimental results, we simulate the carrier dynamics for both InAs and GaAs in magnetic fields ranging from 0 to 8 T. From these simulations, we calculate the amplitude and three-dimensional orientation of the THz emitting dipole. The dipole orientation with respect to the surface of the semiconductor strongly effects coupling of radiation out of the semiconductor.^{18,34} However, knowing the dipole orientation as a function of time, we can calculate the time integrated THz radiation pattern, and hence predict the THz power recorded in experiments.

A. Carrier dynamics

Figure 4(a) shows the simulated time derivative of the current densities in n -type GaAs during and after photoexcitation. The dotted line shows results when there is no magnetic field present [as already presented in Fig. 2(a)]. In this case, the only net acceleration of carriers ($\partial \mathbf{j} / \partial t$) occurs in the z direction. This is clear since the only asymmetries in the system are the surface boundary and surface electric field, both of which are rotationally symmetric about the z axis. The solid lines represent a simulation with a magnetic field of 8 T. The magnetic field breaks the rotational symmetry as a result of the Lorentz force. Hence a net acceleration of carriers is seen in the x - y plane.

Figure 4(a) reveals that there is little change to the strength of the dipole as the magnetic field is increased. However, the x and y components of $\partial \mathbf{j} / \partial t$ show that the dipole is rotated. As will be discussed in the next section, it is this rotation of the dipole, rather than an increase in its strength, which gives rise to the magnetic-field-induced enhancement of THz emission which has been reported experimentally.

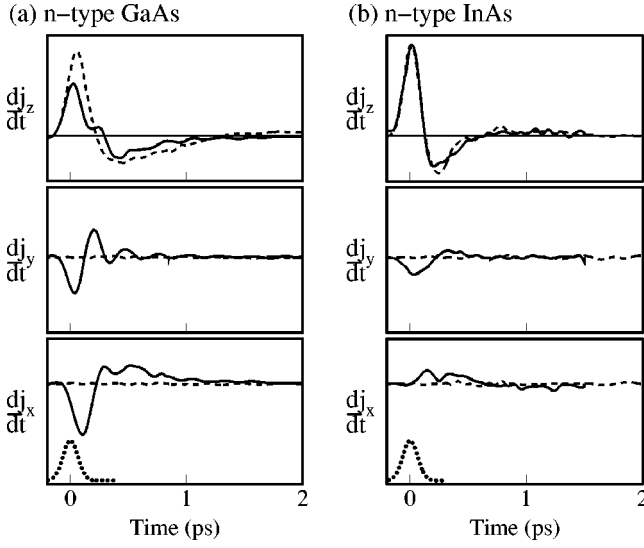


FIG. 4. Three spatial components of the time derivative of average current density for *n*-type (a) GaAs and (b) InAs at $B=0$ (dashed lines) and $B=8$ T (solid lines). The dotted curve represents the intensity profile of the laser pulse. The vertical axis range in (b) is $4\times$ that in (a).

The magnetoplasmon “dispersion” for the GaAs sample is shown in Fig. 5. These results were obtained by running a series of simulations where a δ function replaced the Gaussian laser pulse. Thus all frequency components in the system were excited. Each point in Fig. 5 corresponds to a peak in the Fourier transform of the $\partial \mathbf{j}_y / \partial t$ curves. Magnetoplasmon effects are very important, as can be seen by the large anti-crossing at 2 T. The low-frequency oscillations in Fig. 4(a), and experimental reports,¹⁶ show that the frequency of the emitted THz radiation does not simply follow the cyclotron frequency. This is because the system is excited at low frequencies (with a long ≈ 100 fs Gaussian pulse) and the high-frequency components are heavily damped by phonon scattering. The lower branch of the magnetoplasmon dispersion thus dominates the THz spectra as the magnetic field is increased.

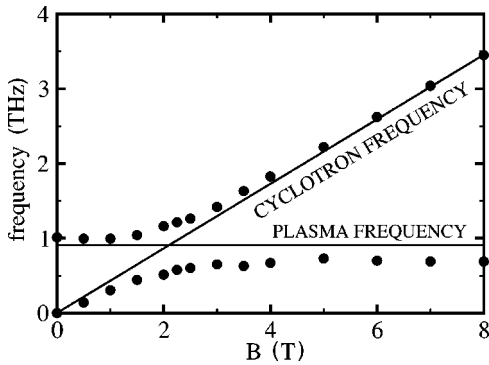


FIG. 5. Magnetoplasmon dispersion curves for *n*-type GaAs. The figure was constructed from a series of simulations where the laser pulse was a δ -function and scattering mechanisms were removed. Points are taken from peaks in the Fourier transforms of each $\partial \mathbf{j}_y / \partial t$ curve (corresponding to the TE-polarized THz radiation in Fig. 1).

Figure 4(b) shows the simulated time derivative of the current densities in *n*-type InAs. As with GaAs, the InAs simulation shows little change in the total dipole strength, and again an 8-T magnetic field induces off z axis components of $\partial \mathbf{j} / \partial t$. However, compared with GaAs the effect is much less pronounced. This is because intervalley scattering is a much more important electron scattering process in InAs excited with 1.55-eV photons. The large effective mass of electrons scattered into the L valleys limits the rotation of the photogenerated dipole, and hence the relative magnitude of the lateral $\partial \mathbf{j} / \partial t$ components. If intervalley scattering processes are excluded from the simulation, or InAs is excited with lower energy photons, we observe a larger dipole rotation. However, it should be noted that inclusion of Γ valley nonparabolicity in the simulation would also limit the rotation of the dipole.

B. Radiation coupling

THz emission from semiconductors is typically detected in free space. However, the radiation is generated from a dipole within a medium with refractive index $n_i \approx 3.5$ and must be transmitted into a medium of refractive index $n_e = 1.0$ in order to be measured. It is clear that any radiation generated outside a cone of about $\theta_i < 17^\circ$ (measured from the surface normal) will be totally internally reflected. In Fig. 6 this cone is shown by the shaded region and several THz rays are added for illustrative purposes.

To calculate the emission pattern resulting from radiation generated within this 17° cone, we consider Fresnel transmission coefficients. For the geometry shown in Fig. 1, the radiation emitted at an angle θ_e from the surface normal is given by

$$E_{TE}(\theta_e, t) \propto \frac{2 \sin \theta_e \cos \theta_i}{\sin(\theta_e + \theta_i)} \left[\frac{\partial J_y}{\partial t} \right], \quad (11)$$

$$E_{TM}(\theta_e, t) \propto \frac{4 \sin \theta_e \cos \theta_i}{\sin 2\theta_e + \sin 2\theta_i} \left[\frac{\partial J_z}{\partial t} \sin \theta_i - \frac{\partial J_x}{\partial t} \cos \theta_i \right],$$

where θ_i is the corresponding internal angle, given by Snell’s law $n_e \sin \theta_e = n_i \sin \theta_i$, with n_e , n_i the external and internal refractive indices. In these expression the prefactors are the Fresnel coefficients and the quantities in the square brackets are proportional to the internal electric fields, $\mathbf{E}_i \propto \partial \mathbf{j} / \partial t$, obtained from Eq. (2) of the simulation.

The radiation pattern (THz power as a function of detection angle θ_e) is obtained from the time integral of the square of the electric fields:

$$P_{TE(M)}(\theta_e) \propto \frac{n_e \cos \theta_e}{n_i \cos \theta_i} \int |E_{TE(M)}(\theta_e, t)|^2 dt. \quad (12)$$

The prefactor, $(n_e \cos \theta_e) / (n_i \cos \theta_i)$, accounts for the differences in the propagation speeds and solid angle elements in the internal and external media.

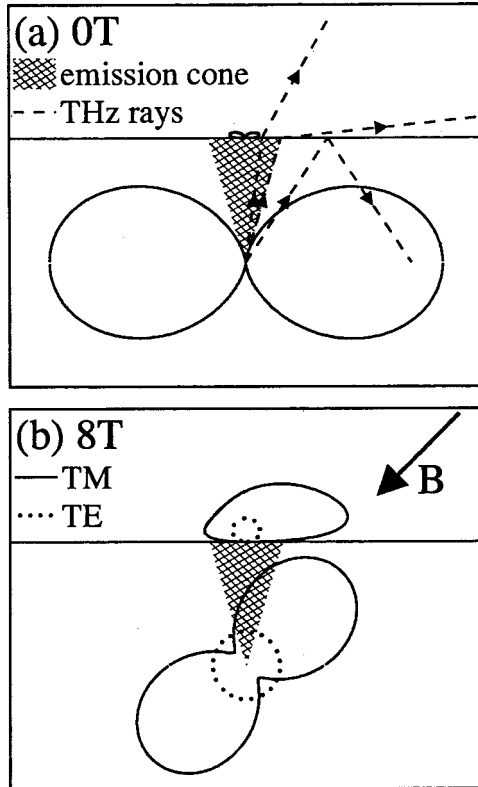


FIG. 6. Calculated polar radiation patterns for GaAs at (a) 0 and (b) 8 T. In each part the horizontal line is a schematic representation of the surface of the semiconductor. The bow tie pattern below the surface line is calculated for radiation within the semiconductor, whereas the pattern above the surface shows the radiation emitted into free-space. The vector B indicates the magnetic-field direction.

The data from the $B=0$ GaAs simulation is presented in Fig. 6(a). The lower “bow-tie” radiation pattern shows the power produced inside the GaAs, whereas the very small pattern above the surface line is the radiation pattern emitted from GaAs into free space. It is clear that the amount of radiation emitted is very low because of the small overlap between the (shaded) emission cone and the internal radiation pattern.

Figure 6(b) is calculated from the $B=8$ T GaAs simulation. The internal radiation pattern shows the rotation of the TM-emitting THz dipole from parallel to the z axis to approximately perpendicular to the magnetic-field vector. A TE component, shown by the dotted line, also emerges as a result of the dipole rotating out of the x - z plane. In this case there is considerable overlap between the internal radiation pattern and the emission cone. Hence, the corresponding free-space radiation pattern is much larger than the case where no magnetic field is applied. For InAs there is only a small rotation of the THz dipole. Thus the enhancement of the free-space radiation pattern is much less.

The enhancement in total THz power emitted at $\theta_e=45^\circ$ between 0 and 8 T has been measured experimentally to be $35\times$ for GaAs (Refs. 13 and 34) and $8\times$ for InAs (Ref. 16) when the detection angle is $\theta_e=45^\circ$. Here, we calculate values of $15\times$ and $4\times$, respectively. These results are in reasonable agreement considering the simplicity of our semi-

classical simulation, and possible differences between simulation and reported experimental parameters. The relative magnitude of the TE and TM components of the simulated GaAs THz emission agree well with experiments,³⁴ however, the InAs simulation produces a smaller TE power component than is observed experimentally. This discrepancy may result from the effects of nonparabolicity in the conduction band of InAs, which our present model does not consider.

It should be noted that these radiation patterns are calculated assuming the the THz emitter is a point dipole. In reality this corresponds to an experiment in which the laser spot is much smaller than the THz wavelength. However, our results are still valid for excitation with larger area, more collimated laser beams, where an ensemble of THz dipoles are coherently generated by the laser wave front. In this case, THz emission is seen primarily in the quasireflection and transmission directions. The radiation patterns presented here are then mapped out by varying the incident angle of the laser α with the detection angle θ_e , ($-90^\circ > \alpha = \theta_e > 90^\circ$).¹³

V. CONCLUSION

We have developed a semiclassical Monte Carlo model which simulates the dynamics of extrinsic and photoexcited electrons and holes on a subpicosecond time scale. This simulation shows that on exciting with a laser pulse, the primary THz emission mechanism from InAs is based on the photo-Dember effect, while surface depletion fields dominate in GaAs.

The effect of magnetic field on these two systems is also calculated using the model. We find that the experimentally observed enhancement of THz power with magnetic field is mainly caused by a reorientation of the THz dipole with respect to the surface dielectric boundary, rather than by an increase in the dipole strength. Once transmission through the semiconductor-air dielectric interface is considered, the experimentally observed enhancement in emission is reproduced. The magnetic-field-induced enhancement in InAs is less than is observed in GaAs because of a smaller dipole rotation.

Our results suggest that a magnetic field is not necessary to obtain the order of magnitude THz power enhancements measured recently. Instead, modification of the orientation of the dipole with respect to the dielectric air interface, by way of a prism or lens, or reduction in the effective refractive index of the semiconductor, should produce a similar level of enhancement. This is potentially important in the quest for compact high power THz emitters.

ACKNOWLEDGMENTS

We acknowledge support from the EPSRC, as well as the High Performance Computing Facility at the University of Cambridge, and, in particular, Dr. G. McMullan. We thank Dr. D. D. Arnone of Teraview Ltd. for help and support. A.G.D. and E.H.L. acknowledge support from the Royal Society, and Toshiba Research Europe Ltd., respectively.

- ¹X.-C. Zhang, B. B. Hu, J. T. Darrow, and D. H. Auston, *Appl. Phys. Lett.* **56**, 1011 (1990).
- ²B. B. Hu, X.-C. Zhang, and D. H. Auston, *Phys. Rev. Lett.* **67**, 2709 (1991).
- ³A. Leitenstorfer, S. Hunsche, J. Shah, M. C. Nuss, and W. H. Knox, *Phys. Rev. B* **61**, 16 642 (2000).
- ⁴R. Kersting, J. N. Heyman, G. Strasser, and K. Unterrainer, *Phys. Rev. B* **58**, 4553 (1998).
- ⁵D. H. Auston and K. P. Cheung, *J. Opt. Soc. Am. B* **2**, 606 (1984).
- ⁶P. Y. Han, G. C. Cho, and X.-C. Zhang, *Opt. Lett.* **25**, 242 (2000).
- ⁷D. M. Mittleman, S. Hunsche, L. Boivin, and M. C. Nuss, *Opt. Lett.* **22**, 904 (1997).
- ⁸R. M. Woodward, B. Cole, V. P. Wallace, D. D. Arnone, R. Pye, E. H. Linfield, A. G. Davies, and M. Pepper, in *Technical Digest of the Conference on Lasers and Electro-Optics* (Optical Society of America, Baltimore, 2001).
- ⁹P. Gu, M. Tani, S. Kono, and K. Sakai, in *8th International Conference on Terahertz Electronics* (VDE Verlag, Berlin-Offenbach, 2000), pp. 63–65.
- ¹⁰S. Kono, P. Gu, M. Tani, and K. Sakai, *Appl. Phys. B: Lasers Opt.* **71**, 901 (2000).
- ¹¹H. Ohtake, S. Ono, Z. Liu, N. Sarukura, M. Ohta, K. Watanabe, and Y. Matsumoto, *Jpn. J. Appl. Phys., Part 2* **38**, L1186 (1999).
- ¹²C. Weiss, R. Wallenstein, and R. Beigang, *Appl. Phys. Lett.* **77**, 4160 (2000).
- ¹³M. B. Johnston, A. Corchia, A. Dowd, E. H. Linfield, A. G. Davies, R. McLaughlin, D. D. Arnone, and M. Pepper, *Physica E* (to be published).
- ¹⁴N. Sarukura, H. Ohtake, S. Izumida, and Z. Liu, *J. Appl. Phys.* **84**, 654 (1998).
- ¹⁵S. Izumida, S. Ono, Z. Liu, H. Ohtake, and N. Sarukura, *Appl. Phys. Lett.* **75**, 451 (1999).
- ¹⁶R. McLaughlin, A. Corchia, M. B. Johnston, Q. Chen, C. M. Ciesla, D. D. Arnone, G. A. C. Jones, E. H. Linfield, A. G. Davies, and M. Pepper, *Appl. Phys. Lett.* **76**, 2038 (2000).
- ¹⁷J. N. Heyman, P. Neocleous, D. Hebert, P. A. Crowell, T. Müller, and K. Unterrainer, *Phys. Rev. B* **64**, 085202 (2001).
- ¹⁸J. Shan, C. Weiss, R. Wallenstein, R. Beigang, and T. F. Heinz, *Opt. Lett.* **26**, 849 (2001).
- ¹⁹S. L. Chuang, S. Schmitt-Rink, B. I. Greene, P. N. Saeta, and A. F. J. Levi, *Phys. Rev. Lett.* **68**, 102 (1992).
- ²⁰X. C. Zhang, Y. Jin, and X. F. Ma, *Appl. Phys. Lett.* **61**, 2764 (1992).
- ²¹X.-C. Zhang, Y. Jin, L. E. Kingsley, and M. Weiner, *Appl. Phys. Lett.* **62**, 2477 (1993).
- ²²X.-C. Zhang and D. H. Auston, *J. Appl. Phys.* **71**, 326 (1992).
- ²³T. Dekorsy, T. Pfeifer, W. Kütt, and H. Kurz, *Phys. Rev. B* **47**, 3842 (1993).
- ²⁴H. Dember, *Phys. Z.* **32**, 554 (1931).
- ²⁵H. Dember, *Phys. Z.* **32**, 856 (1931).
- ²⁶H. Dember, *Phys. Z.* **33**, 207 (1932).
- ²⁷T. Dekorsy, H. Auer, H. J. Bakker, H. G. Roskos, and H. Kurz, *Phys. Rev. B* **53**, 4005 (1996).
- ²⁸A. V. Efanov and M. V. Éntin, *Fiz. Tekh. Poluprovodn.* **20**, 24 (1986) [*Sov. Phys. Semiconductors* **20**, 11 (1986)].
- ²⁹T. Held, T. Kuhn, and G. Mahler, *Phys. Rev. B* **44**, 12 873 (1991).
- ³⁰R. Kersting, K. Unterrainer, G. Strasser, H. F. Kauffmann, and E. Gornik, *Phys. Rev. Lett.* **79**, 3038 (1997).
- ³¹A. V. Kuznetsov and C. J. Stanton, *Phys. Rev. B* **48**, 10 828 (1993).
- ³²A. V. Efanov and M. V. Éntin, *Fiz. Tekh. Poluprovodn.* **22**, 386 (1986) [*Sov. Phys. Semiconductors* **22**, 237 (1998)].
- ³³G. Meinert, L. Bányai, P. Gartner, and H. Haug, *Phys. Rev. B* **62**, 5003 (2000).
- ³⁴M. B. Johnston, D. M. Whittaker, A. Corchia, A. G. Davies, and E. H. Linfield, *J. Appl. Phys.* **91**, 2104 (2002).
- ³⁵W. H. Press, B. P. Flannery, S. A. Teukolsky, and W. T. Vetterling, *Numerical Recipes in C* (Cambridge University Press, Cambridge, England, 1993), code modified into three-dimensions by the author.
- ³⁶K. Tomizawa, *Numerical Simulation of Submicron Semiconductor Devices* (Artech House, Inc., Boston, 1993).
- ³⁷B. K. Ridley, *Quantum Processes in Semiconductors* (Clarendon Press, Oxford, 1993).
- ³⁸O. Madelung, ed., *Semiconductor Basic Data* (Springer-Verlag, Berlin, 1996), 2nd ed.
- ³⁹I. Vurafman, J. R. Meyer, and L. R. Ram-Mohan, *J. Appl. Phys.* **89**, 5815 (2001).
- ⁴⁰S. Zollner, S. Gopalan, and M. Cardona, *Appl. Phys. Lett.* **54**, 614 (1989).
- ⁴¹P. Y. Yu and M. Cardona, *Fundamentals of Semiconductors, Physics and Material Properties* (Springer, Berlin, 1996), Chap. 8, pp. 448–453.
- ⁴²L. A. Balagurov, O. Y. Borkovskaya, N. L. Dmitruk, O. I. Maeva, and E. M. Omel'yanovskii, *Fiz. Tekh. Poluprovodn.* **10**, 1108 (1976) [*Sov. Phys. Semicond.* **10**, 659 (1976)].
- ⁴³S. Ono, M. Takeuchi, and T. Takahashi, *Appl. Phys. Lett.* **78**, 1086 (2001).
- ⁴⁴W. E. Spicer, Z. Liliental-Weber, E. Weber, N. Newman, T. Kendelewicz, R. Cao, C. McCants, P. Mahowald, K. Miyano, and I. Lindau, *J. Vac. Sci. Technol. B* **6**, 1245 (1988).